

# Cosmic ray energy reconstruction from the $S(500)$ observable recorded with the KASCADE-Grande air shower experiment

W.D. Apel<sup>a</sup>, J.C. Arteaga-Velázquez<sup>b</sup>, K. Bekk<sup>a</sup>, M. Bertaini<sup>c</sup>, J. Blümer<sup>a,d</sup>, H. Bozdog<sup>a</sup>, I.M. Brancus<sup>e</sup>, E. Cantoni<sup>c,f,1</sup>, A. Chiavassa<sup>c</sup>, F. Cossavella<sup>d,2</sup>, K. Daumiller<sup>a</sup>, V. de Souza<sup>g</sup>, F. Di Pierro<sup>c</sup>, P. Doll<sup>a</sup>, R. Engel<sup>a</sup>, D. Fuhrmann<sup>h,3</sup>, A. Gherghel-Lascu<sup>e</sup>, H.J. Gils<sup>a</sup>, R. Glasstetter<sup>h</sup>, C. Grupen<sup>i</sup>, A. Haungs<sup>a,\*</sup>, D. Heck<sup>a</sup>, J.R. Hörandel<sup>j</sup>, D. Huber<sup>d</sup>, T. Huege<sup>a</sup>, K.-H. Kampert<sup>h</sup>, D. Kang<sup>d</sup>, H.O. Klages<sup>a</sup>, K. Link<sup>d</sup>, P. Łuczak<sup>k</sup>, H.J. Mathes<sup>a</sup>, H.J. Mayer<sup>a</sup>, J. Milke<sup>a</sup>, B. Mitrica<sup>e</sup>, C. Morello<sup>f</sup>, J. Oehlschläger<sup>a</sup>, S. Ostapchenko<sup>l</sup>, N. Palmieri<sup>d</sup>, T. Pierog<sup>a</sup>, H. Rebel<sup>a</sup>, M. Roth<sup>a</sup>, H. Schieler<sup>a</sup>, S. Schoo<sup>a</sup>, F.G. Schröder<sup>a</sup>, O. Sima<sup>m</sup>, G. Toma<sup>e,\*</sup>, G.C. Trinchero<sup>f</sup>, H. Ulrich<sup>a</sup>, A. Weindl<sup>a</sup>, J. Wochele<sup>a</sup>, J. Zabierowski<sup>k</sup>

<sup>a</sup>Institut für Kernphysik, KIT - Karlsruhe Institute of Technology, Germany

<sup>b</sup>Universidad Michoacana de San Nicolas de Hidalgo, Inst. Física y Matemáticas, Morelia, Mexico

<sup>c</sup>Dipartimento di Fisica, Università degli Studi di Torino, Italy

<sup>d</sup>Institut für Experimentelle Kernphysik, KIT - Karlsruhe Institute of Technology, Germany

<sup>e</sup>Horia Hulubei National Institute of Physics and Nuclear Engineering, Bucharest, Romania

<sup>f</sup>Osservatorio Astronomico di Torino, INAF Torino, Italy

<sup>g</sup>Universidade São Paulo, Instituto de Física de São Carlos, Brasil

<sup>h</sup>Fachbereich Physik, Universität Wuppertal, Germany

<sup>i</sup>Department of Physics, Siegen University, Germany

<sup>j</sup>Department of Astrophysics, Radboud University Nijmegen, The Netherlands

<sup>k</sup>National Centre for Nuclear Research, Department of Astrophysics, Łódź, Poland

<sup>l</sup>Frankfurt Institute for Advanced Studies (FIAS), Frankfurt am Main, Germany

<sup>m</sup>Department of Physics, University of Bucharest, Bucharest, Romania

---

## Abstract

The energy reconstruction at KASCADE-Grande is based on a combination of the shower size and the total muon number, both estimated for each individual air-shower event. We present investigations by a second method to reconstruct the primary energy using  $S(500)$ , the charged particle densities inferred with the KASCADE-Grande detector at 500 m distance from the shower axis. We account for the attenuation of inclined showers by applying the 'Constant Intensity Cut' method and we employ a simulation derived calibration to convert the recorded  $S(500)$  into primary energy. We observe a systematic shift of the  $S(500)$ -derived energy in relation to the earlier published results of the standard reconstruction technique. However, a comparison of the two methods on simulated and measured data shows that this shift appears only for measured data. Investigations show that this shift is mainly caused by the insufficient way simulations (QGSJet-II-2, EPOS-1.99) describe the shape of the lateral density distribution.

**Keywords:** cosmic rays, primary energy, KASCADE-Grande,  $S(500)$ , hadronic interaction models

---

## 1. Introduction

Cosmic rays experiments are mainly concerned with inferring the arrival direction, the energy spectrum and the elemental composition of the primary cosmic radiation. The primary energy spectrum falls steeply

and extends up to  $10^{20}$  eV. Two features are immediately visible in the spectrum, in the form of two spectral index changes. These features produce a shape of the spectrum similar to a bent human leg hence their names: *knee* (steepening of the spectrum) and *ankle* (flattening). The two features are strongly correlated in the models describing their source (e.g. [1, 2]). It is generally accepted that towards the highest energies ( $E_0 > 5 \times 10^{18}$  eV), the component above the ankle is most likely of extragalactic origin [3]. Towards lower energies (i.e.  $E_0 \approx 4 \times 10^{15}$  eV), the knee is caused by a

\*Corresponding authors

Email addresses: andreas.haungs@kit.edu (A. Haungs), gabriel.toma@outlook.de (G. Toma)

<sup>1</sup>now at: Istituto Nazionale di Ricerca Metrologia, INRIM, Torino

<sup>2</sup>now at: DLR Oberpfaffenhofen, Germany

<sup>3</sup>now at: University of Duisburg-Essen, Duisburg, Germany

17 rigidity dependent extinction of the light component in  
 18 the galactic radiation.

19 The KASCADE-Grande [4] experiment has been de-  
 20 signed to record air showers in the  $10^{16}$ - $10^{18}$  eV en-  
 21 ergy range to answer such questions regarding the tran-  
 22 sition to the extragalactic radiation. Recent results at  
 23 KASCADE-Grande [7] show a flux of cosmic rays in  
 24 very good agreement with results of other experiments  
 25 (e.g. KASCADE [5], EAS-TOP [6]). The all-particle  
 26 energy spectrum reported by KASCADE-Grande ex-  
 27 hibits a hardening of the spectrum at  $2 \times 10^{16}$  eV, a knee-  
 28 like feature at around  $8 \times 10^{16}$  eV due to heavy primaries  
 29 and an ankle-like hardening at  $10^{17.8}$  eV due to the light  
 30 component [7, 8, 9]. These results were provided by a  
 31 reconstruction technique based on a  $N_{ch}$ - $N_{\mu}$  correlation  
 32 (i.e. total shower size - muon size) used to infer the  
 33 primary energy from the data recorded by KASCADE-  
 34 Grande.

35 In this paper we present a second approach to re-  
 36 construct the primary energy with KASCADE-Grande.  
 37 This approach is applied independently from the stan-  
 38 dard method and to the same shower sample leading  
 39 to subsequent cross-checks between results. The new  
 40 method is based on a specific primary energy estima-  
 41 tor, the attenuation-corrected charged particle density at  
 42 500 m distance from the shower axis,  $S(500)$ .

## 43 2. KASCADE-Grande

44 The studies in this paper are based on air shower ob-  
 45 servations with the KASCADE-Grande [4] detector ar-  
 46 ray, in particular on measurements of the lateral distri-  
 47 bution of charged EAS particle densities. The array was  
 48 situated at the site of the Karlsruhe Institute of Tech-  
 49 nology - KIT, Campus North, Germany ( $49^{\circ}$  N,  $8^{\circ}$  E)  
 50 at 110 m a.s.l. It had a roughly rectangular shape with  
 51 a length of 700 m (Fig. 1). A complex multi-detector  
 52 system of various types of detectors enabled the regis-  
 53 tration of different EAS observables.

54 Historically, the KASCADE-Grande detector array  
 55 was an extension of a smaller array, KASCADE [5], op-  
 56 erated since 1996. KASCADE was designed to record  
 57 air showers initiated by primaries with energies in the  
 58  $10^{14}$  -  $10^{16}$  eV range (including the knee range whose  
 59 origin to clarify was one of the goals). The KASCADE  
 60 detector was a complex detector array providing infor-  
 61 mation on a considerable number of observables asso-  
 62 ciated with the electromagnetic, muonic and hadronic  
 63 component.

64 The extension of the original smaller but rather de-  
 65 tailed KASCADE array was guided by the intention to  
 66 extend the energy range for efficient EAS detection to

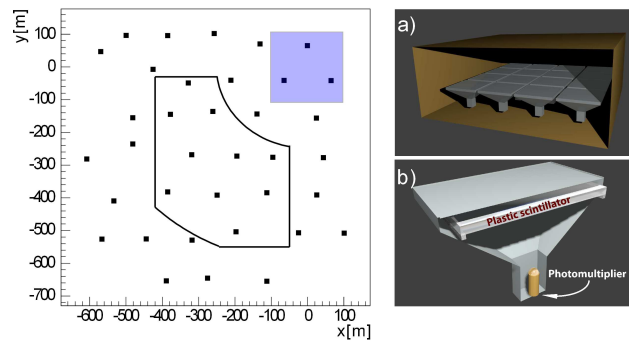


Figure 1: *Left*: schematic top-view of the KASCADE-Grande detector array (the Grande stations are shown as square dots and the fiducial area with line contour, see text) and the area covered by KASCADE (as shaded rectangle); *Right a)* simplified 3D view of the inside of a Grande station; *Right b)* inside view of a scintillator module.

67 the energy range of  $10^{16}$  -  $10^{18}$  eV. This energy range  
 68 provides various interesting aspects: the expected tran-  
 69 sition from galactic to extragalactic origin of cosmic  
 70 rays and, in particular the question whether there ex-  
 71 ists a further knee in the energy spectrum. The layout  
 72 of the extension of KASCADE to KASCADE-Grande  
 73 was governed by following basic considerations. Higher  
 74 energy showers appear with smaller rate. Thus, in or-  
 75 der to record enough events in a reasonable amount  
 76 of time, a larger size of the array was necessary. The  
 77 other aspect arose from the functionality of detectors  
 78 themselves. High energy primaries generate particle-  
 79 rich showers that tend to saturate the detectors close  
 80 to the shower core where the particle density is very high.  
 81 Consequently for a small array, data recorded close  
 82 to the shower core is not reliable and it appears neces-  
 83 sary to extract data from the EAS at greater radial distances.

84 The Grande array consisted of 37 detector stations  
 85 (formerly installed in the EAS TOP array [6]), arranged  
 86 in a roughly hexagonal grid with a spacing of about  
 87 140 m. Each station housed plastic scintillation detec-  
 88 tors organized in 16 units (Fig. 1a) with a total effec-  
 89 tive area of  $10 \text{ m}^2$  per station. The station hut itself  
 90 was made of metal and was placed on the ground. The  
 91 scintillator plates ( $80 \times 80 \times 4$  cm) were arranged in a  
 92  $4 \times 4$  pattern inside each hut. Each plate was enclosed  
 93 in a steel casing of pyramidal shape (Fig. 1b). The  
 94 plate was viewed from below by a high gain photo-multiplier.  
 95 Additionally, the 4 central modules were equipped also  
 96 with low gain photomultipliers. KASCADE-Grande  
 97 was in operation from 2003 until 2013, and is mean-  
 98 while dismantled.

### 99 3. Reconstruction of $S(500)$

#### 100 3.1. $S(500)$ as energy estimator

101 Previous investigations have shown that the charged  
 102 particle density in air showers becomes independent of  
 103 the primary mass at a large but fixed distance from the  
 104 shower axis and that it can be used as an estimator for  
 105 the primary energy [10]. In a comparison between the  
 106 p and Fe initiated showers, the  $e^{+/-}$  excess in p show-  
 107 ers towards lower radial ranges diminishes with the in-  
 108 crease of the distance to the shower axis as the electrons  
 109 get absorbed. At the same time the muon excess in the  
 110 Fe showers gradually becomes more important at larger  
 111 radial ranges. Following this trend, for a given radial  
 112 range this behaviour produces an overlap of the lateral  
 113 distributions (Fig. 2) and in that location the value of  
 114 the charged particle density becomes mass independent.  
 115 Such a distance is specific for a given experiment as it  
 116 depends on the observation level and on the detector  
 117 threshold and sensitivity to the charged particle com-  
 118 ponent. Based on this property a method was derived  
 119 to reconstruct the primary energy from the particular  
 120 value of the charged particle density, observed at such  
 121 specific radial distances. While in the AGASA experi-  
 122 ment the technique was applied for a distance of 600 m  
 123 to the shower axis [11], in the case of the KASCADE-  
 124 Grande array detailed simulations [12] have shown that  
 125 the particular distance for which this effect takes place  
 126 is about 500 m (Fig. 2), hence the notation  $S(500)$   
 127 for the charged particle density at 500 m distance from the  
 128 shower axis. The distance is measured in a plane nor-  
 129 mal to the shower axis and containing the shower core.  
 130 The property of mass independence is visible also in  
 131 Fig. 3 showing the correlation between the energy es-  
 132 timator  $S(500)$  and the primary energy for different pri-  
 133 mary masses.

134 It must be stressed that the properties of the  $S(500)$   
 135 observable are predicted by simulation studies based on  
 136 the QGSJet-II-2 [14] hadronic interaction model and it  
 137 is entirely possible that simulations based on other inter-  
 138 action models could predict different mass-independent  
 139 observables.

#### 140 3.2. Event selection

141 Simulated showers are used for fine tuning the recon-  
 142 struction procedure and also for calibrating the observ-  
 143 able of interest,  $S(500)$  with the primary energy. The  
 144 analysis is applied identically to simulated and experi-  
 145 mental events using the same reconstruction procedure.

146 Air showers are simulated using the CORSIKA [13]  
 147 Monte Carlo EAS simulation tool, with the QGSJet-II-2  
 148 [14] model embedded for high energy interactions. The

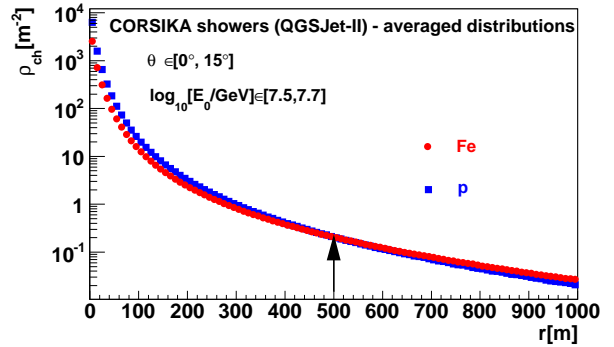


Figure 2: Averaged simulated lateral distributions for p and Fe primaries with energy in a narrow range.

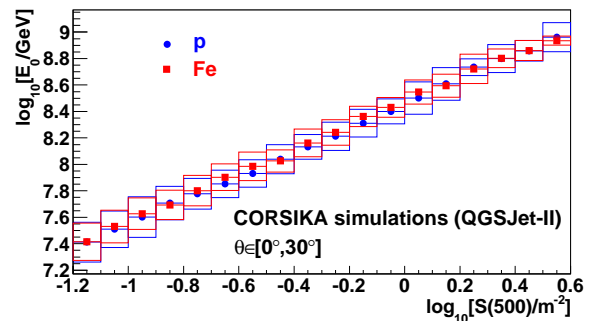


Figure 3: The dependence of the primary energy  $E_0$  on the  $S(500)$  for p and Fe primaries (simulated showers in fairly equal proportions for the two masses); the boxes show the spread of data, the errors on the mean are represented with bars and are dot-sized.

149 set of simulated showers includes events simulated for  
 150 5 primaries (p, He, C, Si and Fe in fairly equal propor-  
 151 tions) with continuous energy spectrum between  $10^{15} -$   
 152  $3 \times 10^{18}$  eV and with a spectral index  $\gamma = -2$  harder than  
 153 the measured data (this allows to faster increase the sta-  
 154 tistical accuracy at higher energies by not simulating as  
 155 many showers at lower energies as in a  $\gamma \approx -3$  sam-  
 156 ple). Since the spectral index of simulations is signifi-  
 157 cantly different from the experimentally observed one,  
 158 a weighting is applied to simulated events in most of  
 159 the subsequent studies to emulate a softer energy spec-  
 160 trum  $\gamma = -3$ . About  $3 \times 10^5$  events have been simulated  
 161 for each primary. The arrival direction of showers is  
 162 isotropical and the shower cores are spread randomly  
 163 on an area larger than the Grande array. In addition, for  
 164 comparisons a smaller set of showers has been simul-  
 165 ated using the high energy hadronic interaction model  
 166 EPOS v1.99 [15].

167 To select a high quality shower sample a set of quality  
 168 cuts is applied identically to the simulated events and to

169 the data. The main requirement is a good reconstruction 220  
 170 of  $S(500)$ , triggering subsequent restrictions for shower 221  
 171 selection: a fiducial area (as shown in Fig. 1), EAS 222  
 172 zenith angle up to  $30^\circ$  and at least 24 triggered stations 223  
 173 in every event. These conditions are intended to mini- 224  
 174 mize geometrical effects due to shower inclinations and 225  
 175 also to reduce the ratio of showers that have no infor- 226  
 176 mation in the lateral density distribution at large radial 227  
 177 ranges. The fiducial area in Fig. 1 has been chosen to 228  
 178 be the same as in [7] in order to increase the similar- 229  
 179 ity of selected shower samples in different primary en- 230  
 180 ergy reconstruction approaches. The fiducial area is a 231  
 181 rectangle omitting the closest and farthest corners re- 232  
 182 lative to the KASCADE array in order to minimize the 233  
 183 under- and overestimation on the muon number which 234  
 184 is relevant for the standard reconstruction approach in 235  
 185 [7]. The acceptance of the experiment under the above 236  
 186 mentioned assumption for fiducial area and zenith an- 237  
 187 gle is  $1.28 \times 10^5 \text{ m}^2 \text{sr}$ . The total acquisition time for 238  
 188 experimental data is 1503 days leading to an exposure 239  
 189 of  $1.66 \times 10^{13} \text{ m}^2 \text{s sr}$ . Approximately  $9.05 \times 10^5$  experi-  
 190 mental events have passed all imposed selection cuts.

### 191 3.3. The reconstruction of $S(500)$

192 The reconstruction procedure that is described in the  
 193 following is applied without any change to both simu- 240  
 194 lated and experimental events [16].

195 The KASCADE-Grande detector stations record the  
 196 energy deposits of particles and the associated temporal  
 197 information (arrival times of particles) without disen- 241  
 198 tangling the particle type (e.g. muons from electrons).  
 199 The temporal information is used to reconstruct the  
 200 zenith and azimuth angles of the shower axis [17]. The  
 201 recorded energy deposit is converted to particle densi-  
 202 ties using appropriate Lateral Energy Correction Func-  
 203 tions (LECF) [18] that take into account the arrival di-  
 204 rection of the shower and the azimuthal position of each  
 205 station around the shower axis.

206 For both experimental and simulated events, the in-  
 207 formation of particle density is usually given in the de-  
 208 tector plane. The shower properties however are bet-  
 209 ter revealed in the plane normal to shower axis. Part-  
 210 icle densities are therefore reconstructed in the plane  
 211 normal to the shower axis [19]. In order to map the  
 212 shower properties from the detector plane onto the nor-  
 213 mal plane, special care was taken in order to avoid dis-  
 214 torting the information. For an inclined shower, the par-  
 215 ticle density around the shower core at a given radial  
 216 range can vary due to different particle absorption and  
 217 scattering in the atmosphere. A relevant example is the  
 218 case of particles propagating directly below the shower  
 219 axis, as opposed to those directly above the shower axis

for an inclined shower. The particles below the axis  
 will travel a shorter distance through atmosphere before  
 reaching the detector level. If detectors are placed pre-  
 dominantly under the shower axis, the particle density  
 would be overestimated (following that in the opposite  
 case the density would be underestimated). Further-  
 more, the angle of incidence of particles in detectors  
 will be different in the two cases because the particles  
 have a transverse momentum and do not propagate par-  
 allel to each other or to the shower axis. The error in the  
 density influences both the reconstructed shower size  
 and the accuracy of shower core reconstruction. A pro-  
 cedure has therefore been introduced in order to com-  
 pensate for the attenuation of inclined showers. In ad-  
 dition the dependence of energy deposits with the angle  
 of incidence of particles is also taken into account.

To calculate the charged particle density at 500 m dis-  
 tance from the shower axis, the lateral density distribu-  
 tion is approximated with a 3-parameter Linsley func-  
 tion (eq. 1,2)[20]<sup>4</sup>:

$$\rho_{ch} = \frac{N}{r_0^2} \cdot C(\alpha, \eta) \cdot \left(\frac{r}{r_0}\right)^{-\alpha} \cdot \left(1 + \frac{r}{r_0}\right)^{-(\eta-\alpha)} \quad (1)$$

where

$$C(\alpha, \eta) = \Gamma(\eta - \alpha) \cdot [2\pi \cdot \Gamma(2 - \alpha) \cdot \Gamma(\eta - 2)]^{-1} \quad (2)$$

with

- 242  $\rho_{ch}(r)$  - charged particle density at distance  $r$ [m] from  
 243 the shower core;
- 244  $N$  - shower size (in this case the total number of charged  
 245 particles);
- 246  $r_0$  - Molière type radius [m];
- 247  $r$  - radius [m];
- 248  $\alpha, \eta$  - two shape parameters.

249 Fig. 4 shows that the ratio of successfully recon-  
 250 structed  $S(500)$  in simulated events exceeds 95% at  
 251 around  $\log_{10}(E_0/\text{GeV}) = 7.5$ . The fluctuations around  
 252 the value 1 for energies  $\log_{10}(E_0/\text{GeV}) > 7.5$  are due  
 253 to the fluctuation of reconstructed shower cores inside  
 254 or outside the fiducial area that is used for shower se-  
 255 lection. In contrast to the  $S(500)$ -based method, the  
 256 full efficiency of the standard reconstruction procedure  
 257 [7] (based on  $N_{ch} - N_\mu$ ) is reached at lower energies,

<sup>4</sup>For applying an independent analysis also a different LDF-  
 function was chosen compared to the standard approach. However,  
 investigations have shown that both functions work equally well in  
 determining  $S(500)$ .

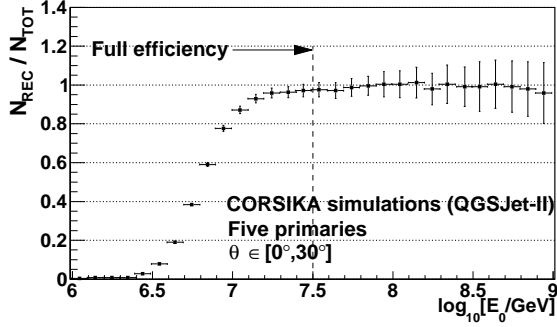


Figure 4: Ratio between the number of simulated events for which  $S(500)$  was successfully reconstructed and the total number of simulated events as a dependence with the primary energy (the energies of the simulated events are distributed as a power law with spectral index  $\gamma=2$ ).

258  $E_0 \approx 10^{16}$  eV. This is mainly due to the shower selection  
 259 procedure (Section 3.2) that is employed to maximize the  
 260 reconstruction quality of  $S(500)$ .

261 The recorded  $S(500)$  values can not be directly converted  
 262 to primary energy without first accounting for the different  
 263 attenuation of inclined events in the atmosphere. This is  
 264 achieved by applying the Constant Intensity Cut (CIC) method  
 265 that corrects all recorded  $S(500)$  values as if the showers  
 266 were coming from a fixed zenith angle (Appendix A). As the  
 267 zenith angular distribution is peaked at  $\approx 21^\circ$ , this value  
 268 was chosen for the CIC reference angle. The measured  
 269  $S(500)$  spectrum is shown in Fig. 5 and the spectrum shows  
 270 similar structures as reported in [7].

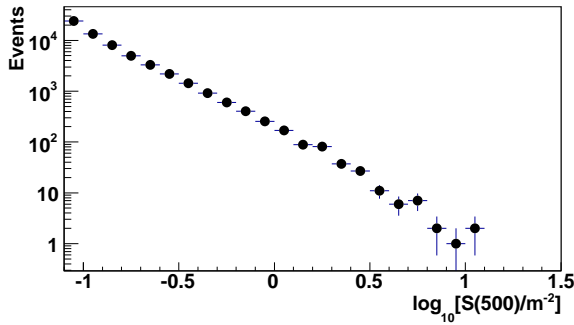


Figure 5: The measured  $S(500)$  spectrum after the CIC correction.

271

### 272 3.4. Energy reconstruction using $S(500)$

A calibration is derived from simulated showers with  
 zenith angle around the CIC reference angle and with a  
 mass composition of 5 primaries in fairly equal proportions  
 (Fig. 6). The calibration is a power law function as

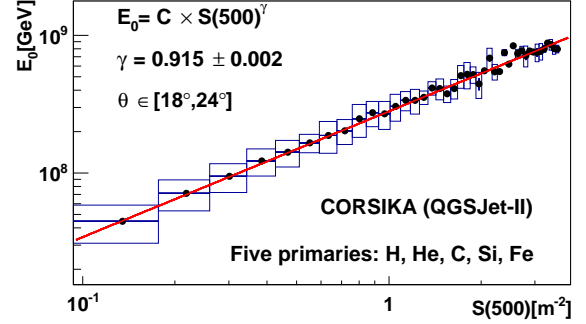


Figure 6:  $E_0 - S(500)$  correlation; the dots are the profile of the scatter plot with box errors showing the spread of data while errors of the mean with simple line are dot sized; the continuous line is a power law fit with  $\gamma=0.915\pm 0.002$ .

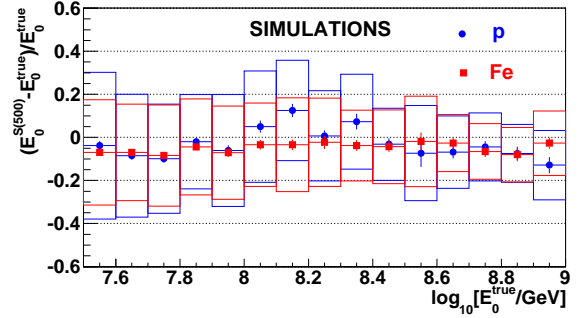


Figure 7: Energy resolution - the box errors show the spread of data while the error of the mean with bar is dot sized; the plot shows the case of p and Fe primaries and a similar behaviour is noted for other primaries too.

in eq. 3 and is used to convert all attenuation-corrected  
 $S(500)$  values to the corresponding primary energy.

$$E_0 = C \cdot S(500)^\gamma \quad (3)$$

273 with  $C$  - a constant; and  $\gamma$  - the slope index of the power  
 274 law dependency.

275 Under the assumptions of the QGSJet-II-2 model the energy  
 276 calibration is found to be composition independent. In order  
 277 to test the method's ability to reproduce the primary energy  
 278 values we calculate the energy resolution. For the simulated  
 279 shower sample we show the relative difference between the  
 280 reconstructed primary energy and the true energy as a  
 281 function of the primary energy (Fig. 7). We then record the  
 282 RMS of the distribution (i.e. energy resolution) for each  
 283 primary energy bin. The energy resolution improves with  
 284 the increase of the energy due to the decrease of shower  
 285 to shower statistical fluctuations at higher energies. Fig. 7  
 286 shows also that there is a slight ( $\approx 5\%$ )  
 287

288 underestimation of the primary energy, more so towards  
 289 lower energies, but still below 10% (this appears in  
 290 the case of small showers where the lateral particle  
 291 density has little or no data towards  $r = 500$  m causing  
 292 the Linsley fit to better describe the range closer to  
 293 the shower core which is much steeper hence leading  
 294 to an underestimation of the density value at 500 m).  
 295

### 296 3.5. Comparison between results

297 In order to ensure that the method based on  $S(500)$   
 298 is working correctly we evaluate the energy reconstruction  
 299 by this and the standard method [7] on an event-by-  
 300 event basis first for simulations and then for data.

301 Figure 8 shows the comparison between the recon-  
 302 structed energy spectra in the two methods and the true  
 303 energy for the same shower sample (in this plot we rep-  
 304 resent the result of each method relative to the true en-  
 305 ergy distribution that is used in simulations). We con-  
 306 clude that for simulated showers both reconstruction  
 307 methods function similarly as the results of each one  
 308 agrees reasonably well with the other.

In the following a similar test is performed for

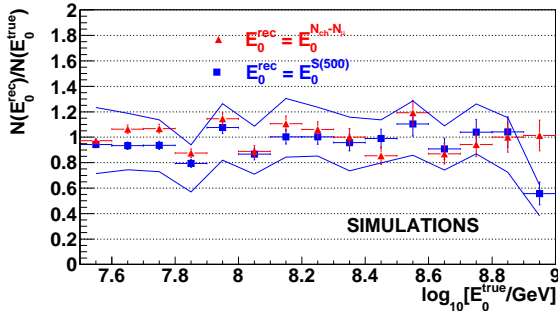


Figure 8: Bin by bin ratio between the reconstructed energy distribution (number of events in each energy bin) and the true energy distribution when reconstructing CORSIKA simulated showers in the two approaches; the continuous lines show the estimated systematic uncertainty for the  $S(500)$ -derived distribution (see Appendix C).

309 experimentally recorded data. In Fig. 9 we plot the ra-  
 310 tio between the reconstructed primary energy from the  
 311 described approach ( $E_0^{S(500)}$ ) and from the standard re-  
 312 construction ( $E_0^{N_{ch}-N_{\mu}}$ ), for an experimental shower sam-  
 313 ple that has been reconstructed by both methods. We  
 314 note that unlike the case of simulations (Fig. 8), for data  
 315  $E_0^{S(500)}$  have systematically higher values (up to 30%)  
 316 than  $E_0^{N_{ch}-N_{\mu}}$ . The difference is not constant over the en-  
 317 tire accessible energy range and seems to diminish at  
 318 the highest energies above  $\log_{10}[E_0^{N_{ch}-N_{\mu}}/\text{GeV}] \approx 8.4$ .  
 319

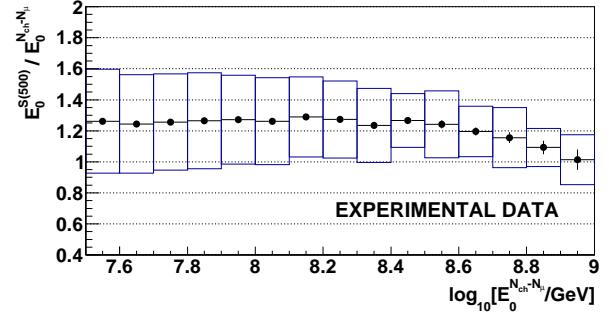


Figure 9: Ratio between the energy from  $S(500)$ ,  $E_0^{S(500)}$  and the reconstructed energy in the standard approach,  $E_0^{N_{ch}-N_{\mu}}$ ; the plot is a profile with box errors showing the spread of data and the bar errors the error of the mean.

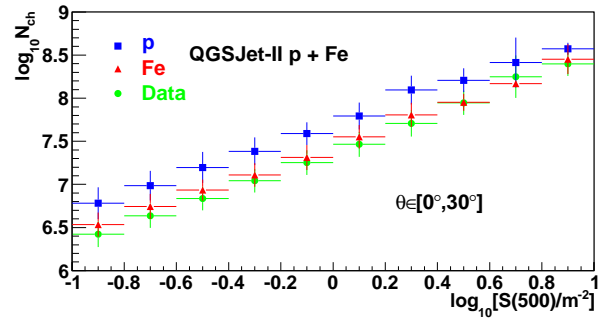


Figure 10: The correlation between the NKG-derived shower size  $N_{ch}^{NKG}$  in the standard approach and the  $S(500)$  for p and Fe simulated events and for experimental data.

320 Applying a correction to the estimated resolution by a  
 321 response matrix (unfolding), the energy spectrum based  
 322 on the  $S(500)$  observable could be determined. But,  
 323 as we observe a systematic shift in the estimated en-  
 324 ergy compared to the standard method applied to the  
 325 KASCADE-Grande detected events, we focus on the in-  
 326 vestigation of the source of this shift. The unfolding  
 327 procedure, the determination of the spectrum, as well as  
 328 the discussion of the uncertainties are described in Ap-  
 329 pendix B and Appendix C.

## 330 4. Discussion

331 Considering that we are using the same procedure  
 332 for the reconstruction of both simulated and experimen-  
 333 tal data, the disagreement between experimental results  
 334 without a corresponding one found in simulated results  
 335 might indicate that certain features of the EAS are not  
 336 described accurately by simulations (such as the shape  
 337 of the lateral distribution, the shower size, the position

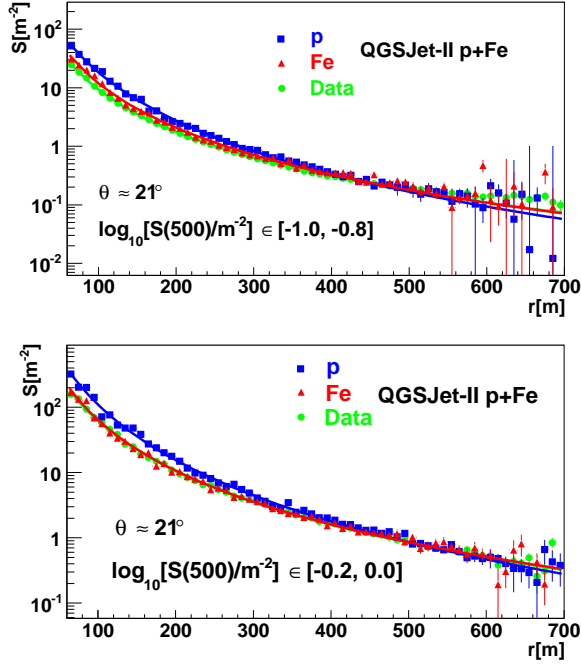


Figure 11: Averaged lateral charged particle density distributions for simulations (CORSIKA/QGSJet-II p and Fe showers) and experimental data, for events with  $\log_{10}[S(500)/\text{m}^{-2}] \in [-1, -0.8]$  (above) and  $\log_{10}[S(500)/\text{m}^{-2}] \in [-0.2, 0.0]$  (below); we show only events inclined at  $\approx 21^\circ$  to avoid effects induced by attenuation in the atmosphere; the continuous lines are of a Linsley-type function.

of the shower maximum or the attenuation of the particle number in the atmosphere). As a test we compare the shower size ( $N_{ch}$ ) for p and Fe simulations and for the experimental data, when selecting showers in the same narrow energy range (selected by same  $S(500)$ ). For showers detected by KASCADE-Grande in the  $10^{16} - 10^{18}$  eV energy range we expect that for a given  $S(500)$  (i.e. fixed energy) the observed  $N_{ch}$  will be in a range delimited by p and Fe assumptions [1, 2]. We use the value of  $N_{ch}$  as inferred on an event by event basis from a modified NKG fit [22] of the lateral distribution as in the standard approach [7] (Fig. 10). For various  $S(500)$  ranges in Fig. 10 we observe that the data does not satisfy the expectations and indicates a mass composition heavier than Fe. This is in agreement with Fig. 11 where we compare averaged lateral density distributions for simulated showers (p and Fe primaries) and data. The experimental lateral distribution is outside the p and Fe predictions towards elements heavier than Fe.

We evaluate this disagreement in a bit more detail. Based on Fig. 10 we impose a change on an event by event basis on the measured  $S(500)$  by decreasing

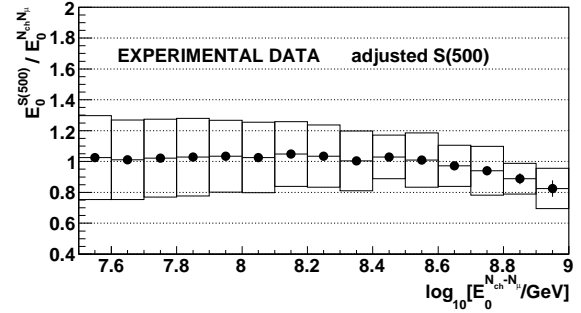


Figure 12: Ratio between the reconstructed energy from  $S(500)$ ,  $E_0^{S(500)}$  and  $E_0^{N_{ch}, N_{\mu}}$ , where the recorded  $S(500)$  is corrected to be in agreement with the QGSJet-II Fe prediction. The box errors show the spread of data and the bar errors the error of the mean.

ing the reconstructed  $S(500)$  values with a value of  $\Delta[\log_{10}S(500)/\text{m}^{-2}] = -0.1$ . The value  $-0.1$  for this correction is the minimum one must introduce in order to satisfy the QGSJet-II-2 (p,Fe) range prediction over the entire energy range accessible to KASCADE-Grande (see Fig. 10). Using the modified experimental  $S(500)$  values the differences in the energy determination vanishes at lower energies (Fig. 12) (and also the resulting spectrum is comparable to the published one within the range of the systematics uncertainties, see Appendix C).

We therefore conclude that the systematic shift between the two KASCADE-Grande results is mainly due to the simulations that do not accurately describe the shape of the lateral density distributions as they appear too steep at large radial ranges in comparison to the data. Since the  $S(500)$ -based method samples most of its information from a reduced radial range at 500 m from the shower axis, it is likely that this method is more sensitive to inaccuracies in the shape of the simulated lateral distribution than the standard approach which samples data from the entire radial range of the lateral density distribution. This is equivalent to saying that a significant (according to Fig. 10 approximately 30% less density) disagreement in shape at 500 m from the shower axis may have significantly less influence on the integrated value  $N_{ch}$ . This picture seems to change at higher energies, where  $S(500)$  is already in the steeper part of the lateral distribution. But as statistics is low, it cannot be decided if 500 m distance is still the appropriate value for an unbiased energy determination.

We discuss in the following two physics possibilities to explain a different lateral shape of charged particles in EAS by simulations and data:

- A shallower lateral density distribution as desired

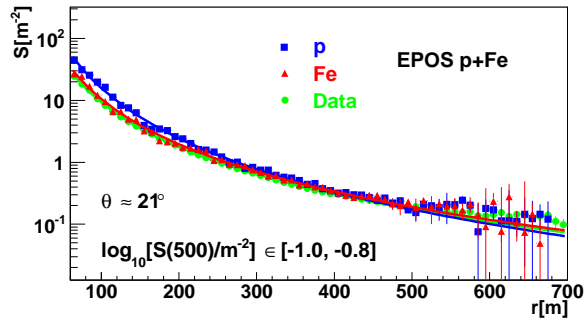


Figure 13: Averaged lateral charged particle density distributions similar to the ones in Fig. 11, but here the simulations are using the EPOS model.

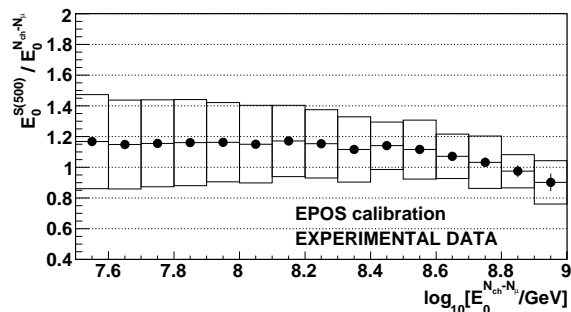


Figure 14: This plot is similar to the one in Fig. 9 but here the  $S(500)$ -derived energy for KASCADE-Grande is inferred using a calibration based on simulations with EPOS.

at large radial ranges is consistent with older showers starting higher in the atmosphere which translates into larger cross section for the primary. This solution however seems to contradict the latest results at LHC<sup>5</sup> [23, 24] that do not encourage further increase of the cross sections in most models. Therefore an even larger cross section for the primary does not seem to be the solution for improving the agreement between data and simulations.

- In a second approach to the matter it seems likely that a higher muon multiplicity resulting in larger number of muons in the shower could increase the curvature of the lateral distribution, given that in the lateral distribution the ratio  $N_\mu/N_{ch}$  is not constant over the entire radial range. At large radial ranges the electron component is practically extinct and the charge component at such ranges is

<sup>5</sup>the particle energy of 900 GeV at the LHC translates in a primary energy of approximately  $10^{16}$  eV of a proton impinging the atmosphere

dominated by muons. An increase in muon multiplicity should therefore have a stronger effect at large radial ranges and produce the desired effect of further *bending* the lateral distribution. We test this hypothesis using a set of CORSIKA simulations based on the EPOS 1.99 hadronic interaction model. One of the differences between EPOS 1.99 and QGSJet-II-2 for a given primary is that on average the EPOS simulated showers will contain more muons (a feature which of course would affect both reconstruction methods at KASCADE-Grande). Fig. 13 shows the averaged lateral density distributions like in Fig. 11 but for simulations based on the EPOS model. With EPOS there seems to be better agreement between data and simulations although experimental data is still not inside the (p, Fe) expected range and the shape is still flatter than for the simulated ones. When deriving the primary energy from  $S(500)$  with a calibration based on EPOS simulations there is indeed a 10% systematic decrease of the primary energy when compared to the case of the QGSJet-II calibration, which reduces the observed difference (Fig. 14), but not vanishes the discrepancies.

In the  $S(500)$ -based method the simulation-derived calibration is very sensitive to the shape of the simulated lateral distribution and even small deviations in the shape of the distributions can have significant effects in the resulting energy spectrum. The same is true when talking about the fluctuations of the  $S(500)$  observable itself. The detected charge particle density at 500 m distance from the shower core can be accompanied by significant fluctuations due to the small number of particles per station or to the fact that in some cases there is no data close to 500 m due to the array size. However, the sensitivity of this method to the shape of the lateral distribution can be turned into a positive feature in evaluating the simulation quality. In contrast to the  $S(500)$ -based approach, the method based on the  $N_{ch}-N_\mu$  correlation infers the primary energy from the whole range of the lateral distribution and is less affected by small deviations in the shape, local fluctuations or the lack of information in the lateral distribution. In this respect, the reconstruction of the primary energy from the charged particle and muon numbers (shower sizes) is more robust.

## 5. Conclusions

The primary energy spectrum of cosmic rays in the range of  $10^{16}$  -  $10^{18}$  eV accessible by the KASCADE-

Grande experiment has been determined based on a correlation between the total number of charged particles and the muon number. In this paper we presented an approach to reconstruct the primary energy of individual measured air-showers based on another energy estimator, the charged particle density at 500 m distance from the shower axis similarly as used in experiments like Auger ( $S(1000)$  [25]), or AGASA ( $S(600)$  [26])<sup>6</sup>. According to the QGSJet-II-2 predictions the  $S(500)$ -derived energy is composition independent as the density of charged particles at 500 m distance to the shower axis is mass-insensitive for the special case of KASCADE-Grande. A study on simulated events preceded the study on experimental data in order to evaluate the reconstruction efficiency and quality and to derive a calibration curve  $E_0 - S(500)$ . The analysis has been applied identically to simulated and experimental events.

The  $S(500)$ -derived primary energy shows a systematic shift when compared to the result of the standard reconstruction approach, but only in case of measured data. In case of simulation both methods result in an energy determination of similar good quality. We explain the origin of this shift in the disagreement between the shape of simulated lateral distributions and the observed distributions. The simulated lateral distributions are too steep at large radial ranges in comparison with the data. The effect seems to be much weaker at higher energies. This might be due to the fact that KASCADE-Grande measures the particle densities up to 700 m core distance only. This can lead to this observation as for higher energies the muons dominate the lateral distributions at larger distances only. The inconsistency between simulations and data is large enough to justify most of the shift between the energy spectra from the two methods. Methodical or detector effects are excluded to be a major effect as several tests were performed like using different lateral distribution functions, independent analysis codes, or the analysis of subsamples of the total shower sample.

We have discussed two possible solutions to improve the agreement between data and simulations. While one solution (higher cross sections) might be disfavored by recent results at the LHC, the possible solution of predicting a higher muon multiplicity seems to be more promising as are the results from preliminary tests based on the EPOS 1.99 interaction model.

<sup>6</sup>It should be noted that in case of the Auger Observatory the calibration of the value is based on calorimetric measurements by the fluorescence telescopes, whereas in case of AGASA or KASCADE-Grande simulations have to be used.

## Acknowledgement

The KASCADE-Grande experiment is supported in Germany by the BMBF and by the Helmholtz Alliance for Astroparticle Physics - HAP funded by the Initiative and Networking Fund of the Helmholtz Association, by the MIUR and INAF of Italy, the Polish Ministry of Science and Higher Education, and the Romanian National Authority for Scientific Research, ANCS-UEFISCDI, project numbers PN-II-ID-PCE-2011-3-0691 and PN-II-RUPD-2011-3-0145. G. Toma acknowledges KIT Karlsruhe for supporting and hosting part of this research activity and also DAAD for supporting part of the study in the frame of the doctoral scholarship A/06/09016 Ref. 322.

- [1] V. Berezhinsky, A. Gazizov, S. Grigorieva, Phys. Rev D 74 (4) (2006) 043005
- [2] A.M. Hillas, J. Phys. G: Nucl. Part. Phys. 31 (2005) R95
- [3] The Pierre Auger, Telescope Array Collaborations, Astrophys. Journ. 794 (2014) 172
- [4] W.D. Apel et al., NIM A 620 (2010) 202-215
- [5] T. Antoni et al. - KASCADE Collaboration, Nucl.Instr. and Meth. A 513 (2003) 429
- [6] M. Aglietta et al. - EAS-TOP Collaboration, Nucl.Instr. and Meth. A 336 (1993) 310
- [7] W.D. Apel et al. (KASCADE-Grande collaboration), Astropart. Phys. 36 (2012) 183-194
- [8] W.-D. Apel et al. (KASCADE-Grande Collaboration), Physical Review Letters 107 (2011) 171104
- [9] W.-D. Apel et al. (KASCADE-Grande Collaboration), Physical Review D 87, 081101(R) (2013)
- [10] A.M. Hillas et al., Proc. 12<sup>th</sup> ICRC, Hobart 3 (1971) 1001
- [11] Y. Dai et al., J.Phys.G: Nucl. Part. Phys. 14 (1998) 793
- [12] H. Rebel and O. Sima et al. KASCADE-Grande collaboration, Proc. 29<sup>th</sup> ICRC Pune India 6 (2005) 297; I.M. Brancus et al. KASCADE-Grande collaboration, Proc. 29<sup>th</sup> ICRC Pune India 6 (2005) 361
- [13] D. Heck et al., Report Forschungszentrum Karlsruhe 6019 (1998)
- [14] N.N. Kalmykov, S.S. Ostapchenko and A.I. Pavlov, Nucl. Phys. B (Proc. Suppl.) 52B (1997) 17-28; S.S. Ostapchenko, Nucl. Phys. B-Proc. 151 (2006) 143-147; S.S. Ostapchenko, Phys. Rev. D 74 (2006) 014026
- [15] K. Werner, F. M. Liu and T. Pierog, Phys. Rev. C 74 (2006) 044902
- [16] O. Sima et al., Report Forschungszentrum Karlsruhe 6985 (2004)
- [17] F. Cossavella et al. - KASCADE-Grande Collaboration, Proc. 30<sup>th</sup> ICRC 2007, Merida, vol. 4, p. 211; R. Glasstetter et al. - KASCADE-Grande collaboration, Proc. 29<sup>th</sup> ICRC 2005, Pune, vol. 6, p. 293
- [18] G. Toma et al., Proc. 26<sup>th</sup> ECRS Lisbon Portugal so-134 (2006); GEANT users guide (1997)
- [19] O. Sima et al. - KASCADE-Grande collaboration, NIM A 638 (2011) 147-156
- [20] J. Linsley et al., Journ. Phys. Soc. Japan 17 (1962) A-III
- [21] T. Antoni et al.: Astrop. Phys. 24 (2005) 1
- [22] W.-D. Apel et al. - KASCADE Collaboration, Astrop. Phys. 24 (2006) 467
- [23] R. Ulrich et al. - Pierre Auger Collaboration, Phys. Rev. Lett. 109, 062002 (2012)

- 569 [24] G. Aad et al., ATLAS Collaboration, 2011, arXiv:1104.0326  
570 [hep-ex]. CMS Collaboration, presentation at DIS workshop,  
571 Brookhaven, 2011  
572 [25] M. Roth et al. - Pierre Auger Collaboration, Proc. 30<sup>th</sup> ICRC  
573 2007, Merida, vol. 4, p. 327  
574 [26] H.Y. Dai et al., J. Phys. G Nucl. Phys. 14 (1988) 793  
575 [27] M. Nagano et al., J.Phys G Nucl.Phys. 10 (1984) 1295  
576 [28] R. Gold, Argonne National Laboratory Report ANL-6984, Ar-  
577 gonne, 1964; H. Ulrich, et al., KASCADE Collaboration, Proc.  
578 27<sup>th</sup> ICRC, Hamburg, 2001.  
579 [29] G.D. Agostini, DESY94-099 (1994); G.D. Agostini, NIM A  
580 362, 1995, p. 487  
581 [30] J. Friedman, Cern School of computing, Norway, 22, 1974  
582 [31] O. Sima et al., "The reconstruction of the lateral charge par-  
583 ticle distributions and the studies of dierent LDF parameteri-  
584 sations", FZKA Interner Bericht KASCADE-Grande 2005-01,  
585 Forschungszentrum Karlsruhe 2005

## 586 Appendix A. The Constant Intensity Cut method

587 Some EAS observables at the detector level are  
588 greatly influenced by the zenith angle of the shower  
589 because, on average, the particles travel along paths  
590 with different lengths in the atmosphere depending  
591 on the zenith angle. Such is the case of the  $S(500)$   
592 which on average can have different values for the same  
593 primaries ( $E_0$ ,  $A_0$ ) arriving from different zenith angles.  
594 One has to correct for this effect before performing an  
595 analysis simultaneously on all recorded EAS events.  
596 This is achieved by applying the Constant Intensity  
597 Cut (CIC) method [27]. The method is based on the  
598 assumption that for a given minimum primary energy  
599 above the full efficiency threshold we should record the  
600 same flux of primaries (i.e. air showers) from all zenith  
601 angles. That is analogous to say that in the integral  
602 spectra from different zenith angles equal intensity  
603 corresponds to the same primary energy.

604 We perform several constant intensity cuts on the  
605 integral  $S(500)$  spectra corresponding to different  
606 zenith angles (Fig. A.15) and for each cut we establish  
607 a correlation between the  $S(500)$  and the corresponding  
608 zenith angle (Fig. A.16). To build the integral  $S(500)$   
609 spectra we pick the zenith angular intervals in the range  
610  $[0^\circ, 30^\circ]$  so that they subtend equal solid angles. We fit  
611 all values in Fig. A.16 simultaneously with a functional  
612 form derived from a second degree polynomial and use  
613 this functional form as a correction function to account  
614 for the attenuation of  $S(500)$ . All reconstructed  $S(500)$   
615 values are corrected by bringing them to the value they  
616 would have at a chosen reference angle. For the present  
617 study the reference angle is considered to be  $21^\circ$ , since  
618 the zenith angular distribution for the recorded EAS  
619 sample peaks at this value. The CIC correction is thus  
620 derived entirely from recorded experimental data and is  
621 independent from simulated studies.

622 The attenuation length  $\lambda_{S(500)}$  of  $S(500)$  is evaluated  
623 using a global fit of the attenuation curves assuming  
624 exponential attenuation (eq. A.1). The resulting value  
625 is  $\lambda_{S(500)} = 402 \pm 7 \text{ g}\cdot\text{cm}^{-2}$ .  
626

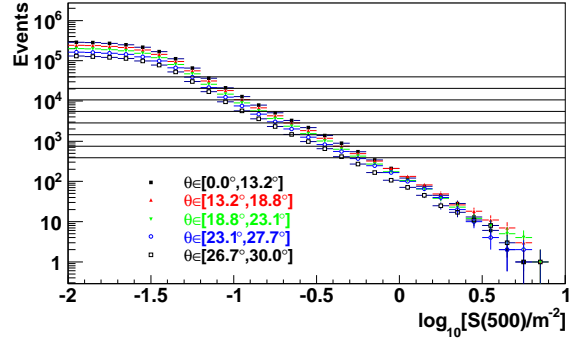


Figure A.15: Integral  $S(500)$  spectra; the horizontal lines are constant intensity cuts at arbitrarily chosen intensities.

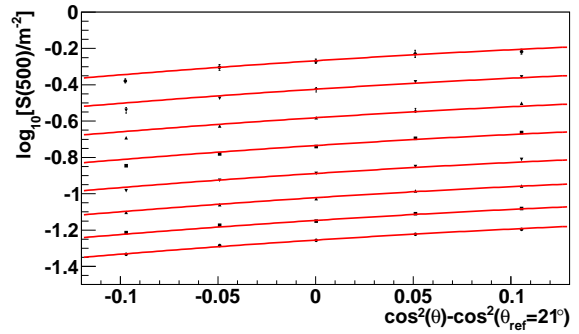


Figure A.16: Variation of the  $S(500)$  observable with the angle of incidence; each set of points correspond to a constant intensity cut in Fig. A.15; the continuous lines show a global fit of all points.

$$S(500)_\theta = S(500)_{\theta_0} \exp \left[ \frac{-h_{\theta_0}}{\lambda_{S(500)}} (\sec\theta - 1) \right] \quad (\text{A.1})$$

## 627 Appendix B. Unfolding based on a response matrix

628 If a given variable is characterized by intrinsic sta-  
629 tistical fluctuations, when representing its spectrum as  
630 a histogram with given bin size, the fluctuations will  
631 cause the total value stored in each bin to deviate from  
632 the true (unknown) value due to events *leaking* to and  
633 from neighbouring bins. In effect, the reconstructed  
634 spectrum is obtained from the true spectrum of the given  
635 variable by folding in each bin the contributions from

636 fluctuations in all neighbouring bins. This migration  
637 depends on the bin size and on the amount of fluctua-  
638 tions and its effects can vary greatly depending on the  
639 spectral shape. This is the case of the reconstructed en-  
640 ergy spectrum which is very steeply decreasing. Given  
641 the steep decrease of the spectrum, it is expected that  
642 contributions into neighbouring bins will have a greater  
643 effect towards higher energies where the flux is much  
644 lower. This affects the flux value and simultaneously  
645 the spectral index and a correction should be applied in  
646 order to compensate. Such a correction is derived us-  
647 ing simulated showers and is based on a response ma-  
648 trix in which we plot the probabilities  $P(E_j^{rec}, E_i^{true})$  that  
649 an energy  $E_i^{true}$  is reconstructed as energy  $E_j^{rec}$  (where  
650  $E_i^{true}/eV \in [10^{16}, 10^{19.5}]$  thus covering the energy range  
651 of interest where such effects are of importance). To un-  
652 fold the effects of fluctuations and infer the true energy  
653 spectrum one has then to solve a system of equations as  
654 eq. B.1.

$$N^{rec}(j) = \sum_{i=1}^{N_{bins}} P(E_j^{rec}, E_i^{true}) N^{true}(i) \quad (\text{B.1})$$

655 where  $\sum_{j=1}^{N_{bins}} P(E_j^{rec}, E_i^{true}) = 1$ .

656 The system is solved iteratively by applying a method  
657 based on the Gold algorithm [28] and then the result is  
658 compared with the result of another approach based on  
659 the Bayes algorithm [29] (applied also iteratively). For  
660 a sufficiently large number of iterations the results of  
661 the two methods converge (Fig. B.17). For each unfold-  
662 ing procedure, a smoothing was applied to the result of  
663 each intermediate iteration in order to avoid fluctuations  
664 amplifying from each iteration to the next. This smooth-  
665 ing was based on the 353HQ-twice algorithm [30]. Ad-  
666 ditionally, the simulation-derived response matrix has  
667 been smoothed in order to reduce the effects induced by  
668 the statistical fluctuations in the Monte Carlo sample.  
669 To smooth the response matrix, the information in each  
670 bin of true energy is fitted with a Gauss-Landau con-  
671 volution and the parameters of the convolution function  
672 are then parametrized with the true energy.

673 The unfolding procedures based on the Gold and  
674 Bayes algorithms were tested by comparing the mea-  
675 sured spectra with the forward folded ones and good  
676 agreement was observed.

### 677 Appendix C. The energy spectrum based on $S(500)$ 678 and its systematic uncertainties

679 The experimental energy spectrum as inferred from  
680 the presented approach is shown as  $E_0^{S(500)}$  in Fig. C.18

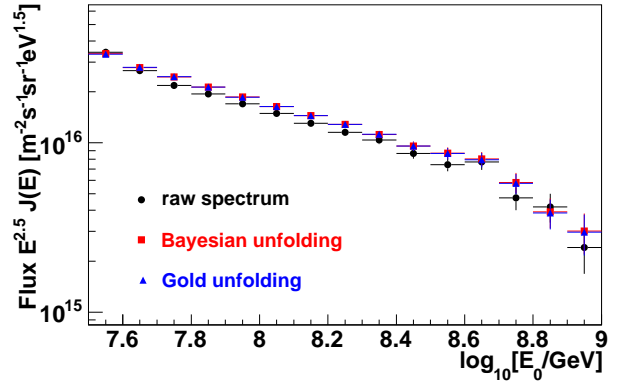


Figure B.17: Results of the Bayes and Gold unfolding algorithms.

681 along with the result of KASCADE [21] towards lower  
682 energies and with the result from the standard approach  
683 [7] as  $E_0^{N_{ch}-N_{\mu}}$ . It is important to note that the KAS-  
684 CADE spectrum is inferred from a procedure using the  
685 QGSJet-01 model for high energy interactions, with dif-  
686 ferent specific systematics than the QGSJet-II-2 used to  
687 infer the two KASCADE-Grande spectra. The figure  
688 shows also the resulting spectrum obtained when using  
EPOS 1.99 as basis for the calibration.

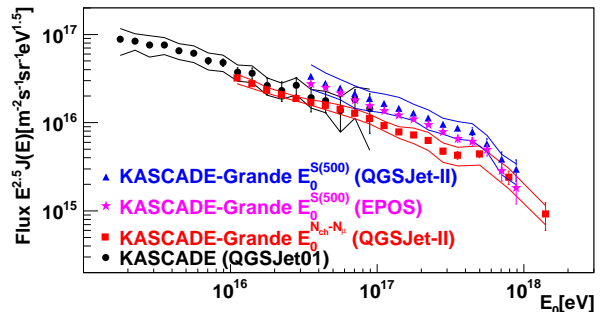


Figure C.18: Primary energy spectra for KASCADE [21] and KASCADE-Grande [7]; the bands with continuous lines show the estimated systematic uncertainty. This plot is similar to the one in Fig. C.18 but here the  $S(500)$ -derived energy spectrum for KASCADE-Grande is inferred using a calibration based on simulations with EPOS.

689 The energy reconstruction procedure implies the use  
690 of complex mathematical procedures that rely on a con-  
691 siderable number of parameters. Certain such param-  
692 eters can vary arbitrarily and lead to fluctuations of the  
693 obtained flux. In order to evaluate the fluctuation in-  
694 duced to the energy flux by each of these factors, they  
695 have been allowed to change and the resulting variation  
696 of energy flux in % was evaluated. We identify such  
697

698 free parameters and estimate their contribution to the 747  
 699 total fluctuation. 748

- 700 • The accuracy of the  $S(500)$  reconstruction. 750  
 701 The  $S(500)$  energy estimator is derived from a 751  
 702 Linsley LDF fit. The quality of this fit is signifi- 752  
 703 cantly affected by the number of stations with good 753  
 704 signal and also by their position inside the lateral 754  
 705 density distribution. The fluctuations in the recon- 755  
 706 structed  $S(500)$  act as a source of uncertainty and 756  
 707 amount to  $\approx 16.5\%$  at  $E_0 = 10^{17}$  eV, decreasing 757  
 708 with energy to  $\approx 8\%$  at  $E_0 = 10^{18}$  eV [31]. 758
- 709 • Uncertainties in the  $E_0 - S(500)$  calibration. 759  
 710 The simulation-derived calibration curve is ob- 760  
 711 tained by a fit procedure and each parameter is 761  
 712 characterized by an uncertainty. In order to evalu- 762  
 713 ate the effects of these uncertainties in terms of sys- 763  
 714 tematics of the energy flux, the fit parameters are 764  
 715 allowed to change according to their uncertainty 765  
 716 and the primary energy spectrum is reconstructed 766  
 717 in this particular new case. The contribution of 767  
 718 this source amounts for a systematic uncertainty of 768  
 719  $\approx 1\%$  at  $E_0 = 10^{17}$  eV, increasing with energy to 769  
 720  $\approx 6\%$  at  $E_0 = 10^{18}$  eV. 770
- 721 • The spectral index of the simulated event sample. 771  
 722 The simulated shower sample that was used 772  
 723 throughout this study was weighted on an event 773  
 724 by event basis to emulate a primary energy spec- 774  
 725 trum with a spectral index  $\gamma = -3$ , close to the 775  
 726 natural index of the cosmic ray spectrum, but not 776  
 727 exactly the same. The reconstruction is repeated 777  
 728 for the cases  $\gamma = -2.8$  and  $\gamma = -3.2$  and the dif- 778  
 729 ference between the fluxes obtained in these two 779  
 730 cases is considered as systematic uncertainty. This 780  
 731 source amounts for  $\approx 2\%$  at  $E_0 = 10^{17}$  eV, increas- 781  
 732 ing slightly with energy to  $\approx 4\%$  at  $E_0 = 10^{18}$  eV 782
- 733 • Influence of the Monte-Carlo statistics on the fit 783  
 734 parameters. 784  
 735 The simulated shower sample used for energy cali- 785  
 736 bration is generated by a Monte Carlo algorithm 786  
 737 which introduces fluctuations differently for differ- 787  
 738 ent energy ranges, since the energy spectrum is a 788  
 739 power law and at high energies there are much less 789  
 740 events available for analysis than at lower energies. 790  
 741 In order to estimate the effect of these fluctuations, 791  
 742 the energy range is divided into 3 sub-ranges and 792  
 743 the energy calibration is performed for every sub- 793  
 744 range. The new parametrizations will vary slightly 794  
 745 from one case to the other due to Monte Carlo fluc- 795  
 746 tuations. The reconstruction is being performed 796

for each particular parametrization and the results  
 are compared. For every energy bin, the differ-  
 ence between the maximum reconstructed flux and  
 the minimum value defines the systematic uncer-  
 tainty from this source. It amount for  $\approx 2\%$  at  
 $E_0 = 10^{17}$  eV, increasing with energy to  $\approx 8\%$  at  
 $E_0 = 10^{18}$  eV

- The systematic error introduced by the CIC.  
 The CIC (Appendix A) method provides an  
 attenuation-corrected  $S(500)$  with an associated  
 uncertainty resulting from the CIC method itself.  
 This acts as another source of systematic uncer-  
 tainty, as the corrected  $S(500)$  is converted to en-  
 ergy. To evaluate the contribution of the CIC  
 method to the overall systematics we allow the cor-  
 rected  $S(500)$  value of each event to change ac-  
 cording to the CIC-specific uncertainty. The con-  
 tribution to the resulting energy flux is rather small,  
 below 1% over the entire energy range.
- Choosing a specific reference angle for which to  
 perform the  $S(500)$  correction of attenuation.  
 When correcting the  $S(500)$  for attenuation, a cer-  
 tain reference angle is chosen. Since the experi-  
 mental zenith angular distribution is peaked at  $21^\circ$ ,  
 the reference angle was chosen to be  $21^\circ$  in or-  
 der to have the CIC method significantly affecting  
 as few showers as possible. However it is possi-  
 ble to choose another angle as well without chang-  
 ing the relevance of the end result, but the correc-  
 tion would affect each shower differently depend-  
 ing on our choice for a reference angle. We are  
 choosing as reference angles the extreme cases  $0^\circ$   
 and  $30^\circ$  and we compare the resulting spectra af-  
 ter applying CIC for these reference angles. The  
 difference between these spectra define the contri-  
 bution of this uncertainty source and it is  $\approx 6\%$  at  
 $E_0 = 10^{17}$  eV increasing to  $\approx 14\%$  at  $E_0 = 10^{18}$  eV.
- The response matrix correction  
 To account for the effect of the statistical fluctua-  
 tions on the energy spectrum, the response matrix  
 correction (see Appendix B) involves very com-  
 plex mathematical operations that are repeatedly  
 applied to the raw recorded energy spectrum. Such  
 operations involve for example fits and smooth-  
 ing. This is an additional source of systematics.  
 To evaluate the contribution of this source we first  
 generate a sample of test spectra. Each of the test  
 spectra is derived by introducing random Poisson-  
 ian noise in the raw un-corrected energy spectrum  
 and then by unfolding it. We forward fold the test

797 spectra (the inverse operation of the unfolding pro-  
798 cedure) and then re-unfold them. We then calcu-  
799 late the average difference between the re-unfolded  
800 spectra and the average of the test spectra. We use  
801 this average difference to define the contribution of  
802 the response matrix correction. It contributes with  
803 about 4% over the entire energy range.

- 804 • Hadronic interaction model.  
805 The combination of QGSJet-II-2 and FLUKA  
806 models has been used for all studies on simulated  
807 events and it is expected that the model itself intro-  
808 duces a systematic effect when describing certain  
809 shower properties. To obtain a rough estimate of  
810 this systematic a second calibration has been de-  
811 rived from simulations based on the EPOS 1.99  
812 model and on average the energy variation with  
813 the new calibration is systematically  $\approx 10\%$  lower  
814 than for QGSJet-II-2. Similarly, when we treat  
815 the EPOS shower sample as experimental data and  
816 reconstruct it using the calibration based on the  
817 QGSJet-II model we obtain a systematic  $\approx 10\%$   
818 overestimation of the energy. This contribution is  
819 only evaluated here, but not included in the sys-  
820 tematic uncertainty band in Fig. C.18, Section 3.4.

821 The above sources (excluding the hadronic interac-  
822 tion models) introduce a combined systematic uncer-  
823 tainty of  $\approx 32\%$  in the energy flux at  $E_0 = 10^{17}$  eV  
824 increasing up to  $\approx 45\%$  at  $E_0 = 10^{18}$  eV.